

EXPERIMENTAL AND NUMERICAL STUDY OF NON-LINEAR INTERACTIONS IN TWO DIMENSIONAL TRANSONIC NOZZLE FLOW

Olivier Bron^{1,2}, Pascal Ferrand¹, and Torsten H. Fransson²

bron@energy.kth.se, Pascal.Ferrand@ec-lyon.fr, fransson@energy.kth.se

¹*L.M.F.A., Ecole Centrale, Lyon, France*

²*Heat and Power Technology, Royal Institute of Technology, Stockholm, Sweden*

Abstract A prerequisite for aeroelastic stability prediction in turbomachines is the understanding of the fluctuating aerodynamic forces acting on the blades. Unsteady transonic flows are complex because of mutual interactions between travelling pressure waves, outlet disturbances, shock motion, and fluctuating turbulent boundary layers. Complex phenomena appear in the shock/boundary layer region and produce phase lags and high time harmonics, which can give a significant contribution to the overall unsteady lift and moment, and therefore affect flutter boundaries, cause large local stresses, or even severely damage the turbomachine.

This paper is concerned with the understanding of phenomena associated with travelling waves in non-uniform transonic flows and how they affect the unsteady pressure distribution on the surface as well as the far field radiated sound. In similitude with turbomachines potential interaction, the emphasis was put on the unsteady interaction of upstream propagating acoustic waves with an oscillating shock in a 2D nozzle flow. Both numerical and experimental studies are carried out and compared with each other. Results showed that the unsteady pressure distribution results from the superposition of upstream and downstream propagating pressure waves, which are partly reflected or absorbed by the oscillating shock. Beside, the phase angle shift underneath the shock location was found to linearly increase with the perturbation frequency, which can be critical regarding aeroelastic stability since it might have a significant impact on the phase angle of the overall aerodynamic force acting on the blade and shift the aerodynamic damping from stable to exciting.

Keywords: Unsteady flow, shock motion, Shock Boundary Layer Interaction, Nozzle flow

Introduction

Transonic flows about streamlined bodies are strongly affected, particularly near the shock location, by unsteady excitations. Experimental and computational studies [1, 2] have shown that the unsteady pressure distribution along the surface of an airfoil or a cascade blade in unsteady transonic flow exhibits a significant bulge near the shock location. Tijdeman and Seebass [3] reported that the unsteady pressure bulge and its phase variation resulted from non-linear interaction between the mean and unsteady flows. This non-linear interaction causes a shift in the shock location, which produces the observed large bulge in the unsteady pressure distribution. Studies [4] on choked flutter have shown that, in unsteady transonic flows around a single airfoil, the shock motion, and thus the pressure distribution along the surface, can be critical regarding to the self-exciting oscillations of the airfoil. It was also shown that the mean flow gradients are of high importance regarding the time response of the unsteady pressure distribution on the airfoil surface. Beside, numerical computations [5] pointed out that the exact location of the transition point could strongly affect the prediction of stall flutter. Further studies [6] suggested that this sharp rise in the unsteady pressure distribution was due to the near sonic condition, and that the near-sonic velocity acts as a barrier they identified as acoustic blockage preventing acoustic disturbances from propagating upstream in a similar way to the shock in transonic flows. A transonic convergent-divergent nozzle experimentally investigated by Ott et al [7] was thereafter used as a model to investigate the non-linear acoustic blockage. Analytical and numerical computations [8–11] were then carried out to analyze and quantify the upstream and downstream propagation of acoustic disturbances in the nozzle.

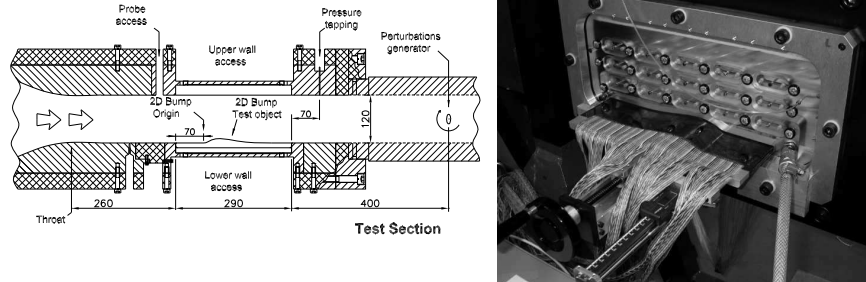
Similarly, in order to focus the present analysis on essential features, the investigation has been carried out in a simple geometry such as a 2D convergent divergent nozzle. Special influences of leading and trailing edges, and interblade row region interactions are therefore avoided.

1. Experimental model

Test facility

The test section was designed highly modular to be able to insert different test objects, so called 'bumps', in a 100x120mm rectangular channel as sketched in figure 1(a). A continuous air supply is provided by a screw compressor driven by a 1MW electrical motor and capable of reaching a maximum mass flow up to 4.7 kg/s at 4 bar. A cooling system allows a temperature range from 30°C to 180°C. The adjustment of different valves also allows the experimentalist to control independently the mass flow and the pressure level in the test section in the respective range of $M_i = 0.1 - 0.8$ and $Re = \frac{\rho_{air} U_{\infty} d}{\nu_{air}} =$

$1.87 \cdot 10^4 - 1.57 \cdot 10^6$ with $d = 0.26\text{m}$, $\rho_{air} = 0.54 - 4.48 \text{ kg/m}^3$ and $\nu_{air} = 1.5 \cdot 10^{-5} \text{ m}^2/\text{s}$.



(a) Modular test section

(b) Traverse mechanism for 2D bump

Figure 1. Transonic wind tunnel test section facility

Test object and instrumentation

The investigated test object consists of a long 2D bump, presented in figure 1(b), which can slide through the width of the test section using the traverse mechanism and inflated O-ring sealing system. The nozzle geometry thus consists of a 100mm wide and 120mm high flat channel with a 10.48mm maximum thickness and 184mm long 2D bump on the lower wall. The beginning of the curvatures was chosen as the origin of the X-axis ($x=0\text{mm}$). The Y-axis and Z-axis were set to be aligned with the channels' width and height respectively to form an orthogonal basis. The profile coordinates of the bump are presented in table A.1.

The bump is equipped with one row of 100 hot film sensors, and three staggered rows of 52 pressure taps each. The traverse mechanism fixed on the side window allows the displacement of both the pressure tap rows and the hot film sensors through the width of the channel. As a result, by sliding the 2D bump and successively position each rows of pressure taps at the same location in the channel will provide a spatial resolution measurements of 1.5mm for pressure measurements. Unsteady pressure measurements were performed using fast response Kulite transducers glued in protective pipes. Each pipe was designed with a locking device so that it could be inserted in any of the already instrumented pressure hole located underneath the sliding 2D bump.

Unsteady perturbation generator

With the aim at simulating potential interaction in turbomachines, the "quasi steady" shock wave was put into oscillations using a rotating elliptical cam placed at $x=625\text{mm}$ in the reference system of the bump. A DC motor was used to rotate the cam up to 15,000RPMs in order to generate pressure perturbations up to 500Hz. The rotating speed was monitored using an optical encoder located directly on the shaft of the motor. Rotating speed fluctuations and time drift were measured under $\pm 0.024\%$ in the worst case. Furthermore,

a TTL pulse generated by the motor was used as a reference signal during unsteady pressure measurements and Schlieren visualizations in order to correlate both measuring techniques.

Measuring techniques

Steady state pressure measurements were performed using a 208-channels 'low speed' data acquisition system. The scanners used feature a pressure range of $\pm 100kPa$ relative to atmosphere with an accuracy of $\pm 0.042\%$ full scale. Taking into account the digital barometer, the overall accuracy for steady state pressure measurements is about $\pm 43.5Pa$. The sampling frequency and sampling time were respectively set to 10Hz and 200s in order to 'capture' the lowest frequencies.

Additionally, a 32-channels high frequency data acquisition and storage system was used for **unsteady pressure measurements**. Accounting for the resonance frequency of the capillarity pipes between the bump surface and the transducer, the sampling frequency was set to 8kHz with a low pass filter at 4kHz to avoid bias effects. Each channel was connected to a fast response Kulite transducer and individually programmed to fully use the 16bit AD conversion. A static calibration of all fast response transducers was performed prior and after the measurements in order to reduce the systematic error related to the drift of the sensitivity and offset coefficients. Furthermore, a dynamic calibration was performed on all pressure taps in order to estimate the damping and time delay of propagating pressure waves through the capillarity tubes. The unsteady pressure measurements were thereafter corrected to account for the above estimated damping and phase-lag.

Finally, a **conventional Schlieren system** connected to a high speed CCD camera was used to monitor the shock motion throughout the whole test section height up to 8kHz. A special feature of the camera allows the display of the TTL signal position directly onto the pictures for referencing purpose during later post treatment. The sampling frequency and shutter speed of the camera were optimally set up depending on the perturbation frequency in order to obtain approximately 20 pictures per unsteady cycle (up to 500Hz). The spatial accuracy based on the camera resolution and optical system was estimated to be around $\pm 0.33mm$. However, it should be reminded that the processed image is an integration of density gradients throughout the channel's width.

Acquisition procedure and data reduction

Steady state operating flow conditions were set up by adjusting the inlet total pressure, inlet total temperature, and outlet static pressure. Both stagnation pressure and temperature were measured in the settling chamber using a total pressure probe and a T-type thermocouple which gave an accuracy of $\pm 0.7K$ on the temperature reading. The outlet static pressure was measured using

a pressure tap located on the upper and side walls at $x=290\text{mm}$. Unsteady operating flow conditions were thereafter estimated by measuring the change in back pressure between the extreme positions (vertical and horizontal) of the downstream rod and then setting the averaged value order to match the steady state operating point. The experimental operating conditions are summarized in table 1.

Table 1. Operating conditions during steady and unsteady pressure measurements

	P_t^{in} [kPa]	T_t^{in} [K]	P_s^{out} [kPa]	M^{in} [-]	\dot{Q}_m [kg/s]
Estimated accuracy	$\pm 43.5 Pa$	$\pm 0.7 K$	$\pm 43.5 Pa$	± 0.001	$\pm 0.03 kg/s$
Steady State OPs*	160.09	303.1	106.07	0.702	3.66
Unsteady measurements**					
• Vertical Rod	160.10	303.3	103.76	0.692	3.73
• Horizontal Rod	160.29	303.4	108.00	0.688	3.73
• Averaged	160.19	303.35	105.88		
Unsteady conditions:	$A_p = \pm 2.12 \text{kPa}$		$F_p = 50, 100, 250, 500 \text{Hz}$		

*Without elliptical rod **With elliptical rod in extreme position

Once the operating conditions were set up, the acquisition procedure for unsteady pressure measurements basically consisted in sliding the 2D bump throughout the width of the channel and record the transducer output voltage together with TTL reference signal for each of the operating conditions summarized in table 1. Schlieren visualizations were performed at the very same operating conditions. As the resolution of the CCD camera decreases with the frame rate, a translation device was used in order to focus the image onto the region of interest in the test section. As a result, shock motion were recorded throughout the whole channel's height.

The data reduction for unsteady pressure measurements consisted of, first, converting the output voltages from the transducers into pressure signals using the coefficients obtained during the static calibration. An ensemble average (EA) of the time-serie data was then performed for each channel using the reference TTL signal from the motor. The obtained single unsteady cycle hence represents an average of all unsteady cycles. Thereafter, a Discrete Fourier Serie Decomposition (DFSD) was performed on the EA signal computed previously and the amplitude and phase angle of the few first harmonics were evaluated. Additionally, a Fast Fourier Transform (FFT) was performed on the entire time fluctuating signal to evaluate all frequency components. At this point, the transfer function (TF) throughout each capillarity tube was evaluated depending on the respective amplitude of the fundamental and finally, both the DFSD components (amplitude and phase of all harmonics) as well as the FFT signal (amplitude only) were corrected using the damping and phase lag values evaluated at the corresponding frequency.

The data reduction procedure for high speed Schlieren visualizations con-

sisted in extracting the instantaneous shock position at different location of the channel's height, perform an EA to obtain a single unsteady cycle and conduct an harmonic analysis on the resulting time-serie signal.

Finally, all data was made dimensionless by dividing the amplitude of each harmonic of the DFSD on pressure by the amplitude of the fundamental at the outlet, and subtracting the phase angle of the outlet pressure signal for each harmonic respectively. As a result, the data issued from harmonic analysis presented in this paper actually corresponds to the pressure amplification and phase lag relative to a reference at the outlet.

2. Numerical model

CFD tool

Simulations were performed using the computational model referenced as PROUST [12] and developed to simulate steady and unsteady, viscous and inviscid flows. The fully three-dimensional unsteady, compressible, RANS equations are solved. The space discretization is based on a MUSCL finite volume formulation. The convective fluxes are evaluated using an upwind scheme based on Roe's approximate Riemann solver, and the viscous terms are computed by a second order centered scheme. The turbulence closure problem is solved using Wilcox $k-\omega$ two equations model and fully accounts for the effect of the boundary layer (BL) separation which originates at the shock foot location. Compatibility relations are used to account for physical boundary conditions. One-dimensional numerical boundary conditions are implemented by retaining the equations associated to the incoming characteristics and fixing the wave velocity to zero to prohibit propagation directed into the computational domain. The resulting semi discrete scheme is integrated in time using an explicit five steps Runge-Kutta time marching algorithm.

Numerical domain

The computed configuration is the experimental 2D nozzle previously described. The numerical domain was however extended 70mm upstream and 164mm downstream of the bump in order to avoid numerical interaction with the boundaries. Steady state simulations were performed on both 2D and 3D structured H-grids in order to achieve a good understanding of the mean flow structures. The respectively meshes comprise 150x84 and 150x84x35 nodes with adapted grid density both around the shock location and in upper, lower and side wall BLs (containing respectively 33, 28 and 26 nodes). Unsteady simulations were however only performed on the 2D mesh due to computation time restriction. Both RANS and Euler unsteady computations were performed for comparison purposes.

Steady flow conditions

For RANS computations, the fluid is modelled as a viscous perfect gas. The specific heat ratio equals $\kappa=1.4$ and the perfect gas constant is $R=287$ J/kg/K. The laminar dynamic viscosity and the thermal conductivity are assumed constant and respectively equal $\mu=1.81 \cdot 10^{-5}$ kg/m/s and $k=2.54 \cdot 10^{-2}$ m.kg/K/s³. The inlet conditions in the free stream are such that the stagnation pressure, P_t^{inlet} , and the stagnation temperature, T_t^{inlet} , equal respectively 160kPa and 303K. A fully developed 7mm thick BL profile computed over a flat duct is specified as inlet condition. The outlet static pressure was adjusted in order to match the experimental shock configuration. The numerical operating conditions are summarized in table 2.

Table 2. Numerical operating conditions

	P_t^{in} [kPa]	T_t^{in} [K]	P_s^{out} [kPa]	M^{in} [-]	\dot{Q}_m [kg/s]
Steady state simulations:					
• 3D RANS	160	303	108	0.695	3.93
• 2D RANS	160	303	110	0.693	3.99
• 2D Euler	160	303	115	0.683	4.02
Unsteady simulations*: $A_p = \pm 2\% P_s^{out} = \pm 2.2$ kPa $F_p=100, 500, 1000$ Hz					

*2D RANS OP

Unsteady flow conditions and data reduction

The shock motion was imposed by sinusoidal downstream static pressure plane fluctuations. The amplitude and frequency of the perturbations are summarized in table 2 and the corresponding reduced frequency are presented in table 3. The reduced frequency based on the BL thickness is considered small enough to justify a quasi-steady response of the turbulence that is compatible with the turbulent model used.

Table 3. Numerical reduced frequency

	100Hz (Based on $L_{bump} = 184$ mm)	500Hz	1000Hz	100Hz (Based on $\delta_{BL} = 7$ mm)	500Hz	1000Hz
k_1	0.5	2.5	5	0.019	0.095	0.19
k_2	0.46	1.16	2.33	0.017	0.044	0.089

NB: $k_i = \frac{2\pi f L}{U_i}$ with $U_1 = 231.2$ m/s or $U_2 = 248.3$ m/s

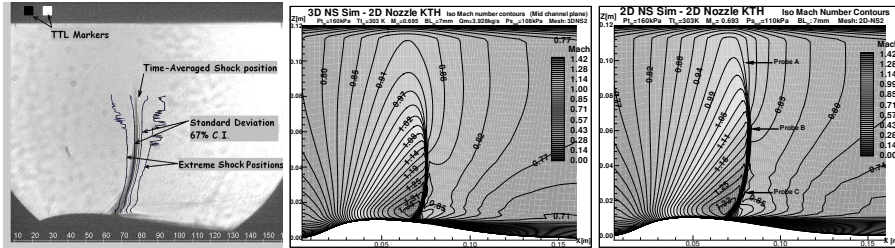
The data reduction consisted in performing an harmonic analysis on both the unsteady pressure distribution and the shock motion. Similarly to experiments, the amplitude of each harmonic was divided by the amplitude of the fundamental at the outlet, and the phase angle value at the outlet reference location was subtracted to all signals, for each harmonic respectively.

3. Results and discussion

Steady state results

The steady state shock wave in the 2D nozzle is presented in figure 1.3.0 for experimental visualization and viscous numerical simulations (at mid channel plane for the 3D RANS simulation). Although a fairly good agreement on the shock location and structure is achieved, the experimental shock position could only be matched by raising up the outlet static pressure value in the numerical simulations. For the same back pressure value, the simulations would position the shock more downstream in the diffuser. Although there might be a real probability that the $k - \omega$ turbulent model underestimates the level of losses, it cannot, by itself, explain the differences in the shock location. A more probable explanation involves the thickening of the side wall BLs and the resulting change in the effective section area, which would act like a slight convergent and magnify the pressure gradient. As the back pressure is manually setup, the pressure right downstream of the shock is then higher and the shock moves upstream.

Using the continuity equation at the outlet ($\dot{Q}_m = \rho_2 V_{x_2} S_2$), the reduction of section area due to BL thickening can be estimated for numerical simulations by calculating the change of section necessary to obtain the experimental mass flow under the same numerical outlet conditions. For the 2D RANS simulation, in which no side wall BL is specified, the change of section area was estimated around 9.44cm^2 , equivalent to a BL with a displacement thickness of 3.9mm on each side wall. For the 3D RANS, which already features outlet side wall BLs, the change of section area was estimated around 7.63cm^2 and is equivalent to an increase of the displacement thickness of 1.73mm on each side wall BL.



(a) Schlieren ($P_{s_{out}}=106\text{kPa}$) (b) 3D RANS ($P_{s_{out}}=108\text{kPa}$) (c) 2D RANS ($P_{s_{out}}=110\text{kPa}$)

Figure 2. Steady state shock structure in 2D nozzle

The steady state pressure distribution at mid channel ($y=50\text{mm}$) over the 2D bump surface is plotted in figure 3 for experimental results and viscous numerical simulations. Although the curves collapse fairly well regarding the shock location, they differ downstream of it. Indeed, experimental results present a smoother pressure recovery, which denotes a change of local curvatures (towards a more convex surface) usually due to a separated flow region. This

phenomenon is even stronger closer to the wall (see pressure distribution at $y=10\text{mm}$) and denotes a large BL thickening or a separation of the flow in the corners. Probably due to larger side wall BLs and the interaction with the shock, the pressure rise occurs more upstream in the region close to the side walls.

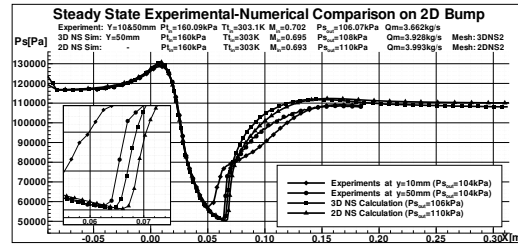
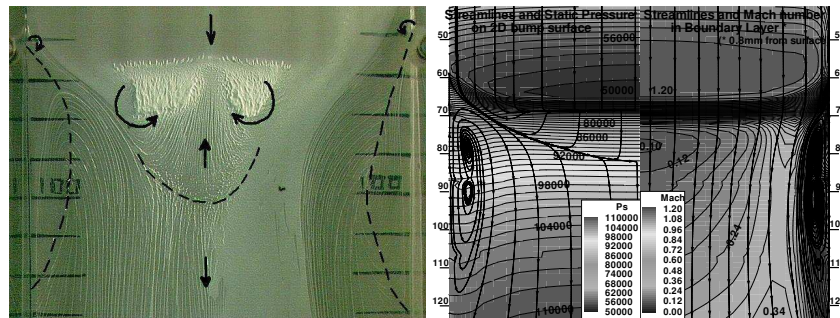


Figure 3. Steady state pressure over 2D bump

Table 4. Separated region location

	X_{sep} [mm]	X_{reat} [mm]	L_{sep} [mm]
Oil visu	67	101	34
3D RANS	68.5	82.0	13.6
2D RANS	70.2	100.2	30

In figure 4 are presented the streamlines from experimental visualization and 3D RANS calculation. As mentioned previously, the side wall BLs start thickening right downstream of the shock and a 15mm large and 60mm long separation appears in both corners. In comparison, the 3D RANS predicts a much lower separated region, both in the corner and at mid channel. Again, this can be an effect of mismatched inlet boundaries or an important underestimation of the losses by the turbulent model. The size of the separated region, measured at mid channel, is presented in table 4. Whereas the 2D RANS calculation presents a fairly good estimation of the separated region, it is noteworthy that the 3D RANS simulation actually gives a much worth prediction. A possible reason might simply be the underestimation of the side wall BL thickening.



(a) Oil-paint ($P_{s_{out}}=106\text{kPa}$)

(b) 3D RANS ($P_{s_{out}}=108\text{kPa}$)

Figure 4. Steady state streamlines over 2D bump

Unsteady results

Numerical-Experimental comparison on unsteady pressure distribution.

The amplitude (normalized by outlet value) and phase angle of the unsteady pressure distribution is plotted in figure 5 for a perturbation frequency of 100Hz. A pressure amplification of factor three can be observed downstream

of the shock location for both experimental and RANS calculation results. It is interesting to note that this amplification is not observed in the Euler simulation and might thus originate viscous or turbulent effects, or even possibly the Shock Boundary Layer Interaction (SBLI).

The analysis of the phase angle distribution is facilitated by considering the behaviour of travelling pressure waves in duct flows. Similarly to potential interaction in turbomachines, outlet static pressure fluctuations propagate upstream at a relative velocity of $U_c - U$. As long as the propagating speed is unchanged, the slope of the phase angle also remains constant, which is the case in the outflow region. However, in the vicinity downstream of the shock, the phase angle stops decreasing and even increases, which would actually correspond to a downstream propagating pressure wave.

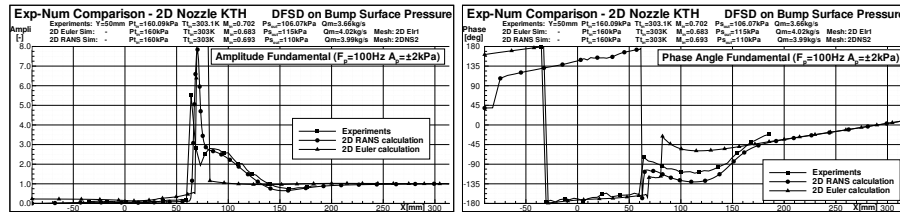


Figure 5. DFSD on unsteady pressure distribution over 2D bump for $F_p=100\text{Hz}$

At higher perturbation frequency ($F_p=500\text{Hz}$ on figure 6), the pressure amplification for both experimental and 2D RANS simulation exhibits an attenuation downstream of the shock whereas the phase angle distribution presents an important phase shift (about 160°) at the same location ($x=95\text{mm}$). Furthermore the same "increasing phase angle" behaviour is still observed downstream of the shock. It is noteworthy that the Euler simulation differs both in the amplitude and phase distribution and does not present the same characteristics.

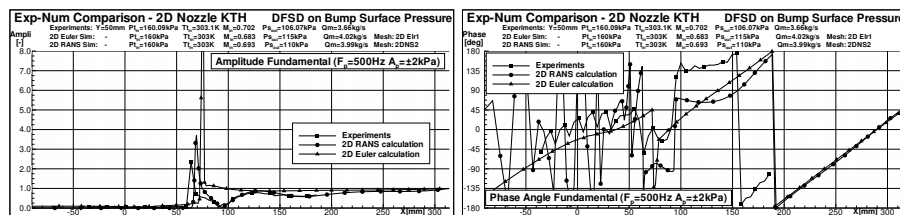


Figure 6. DFSD on unsteady pressure distribution over 2D bump for $F_p=500\text{Hz}$

Generally, a fairly good agreement was achieved between experiments and turbulent computations. However, although the phase angle distribution for experimental measurements and 2D RANS simulation are very similar, there seems to be an "offset" between the two distributions. This may be explained by the location of the experimental reference on the side wall. As the pressure perturbations are generated by the rotating ellipse and propagate upstream in the test section, there might be a possibility of a phase shift between the lower

and side wall pressure measurements as the flow is non uniform in the diffuser downstream of the shock.

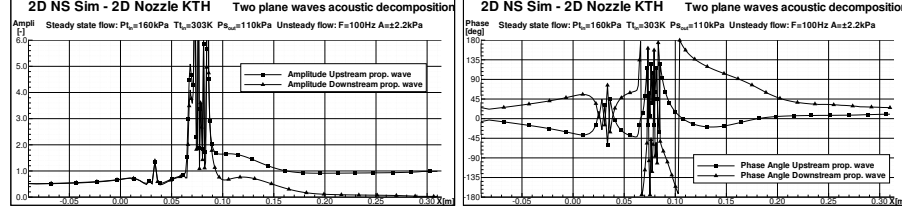


Figure 7. Upstream and downstream propagating plane waves decomposition

Considering the above observation on phase shift (increasing phase angle in the vicinity of the shock) it is believed that the unsteady pressure distribution at this location results from the superposition of an upstream and downstream travelling wave with respective varying amplitudes and phase angles. Assuming that only plane waves can propagate in the nozzle at 100Hz, a one dimensional acoustic decomposition (see equation 1) was performed on the 2D RANS numerical results using the isentropic flow velocity and sound speed on the bump surface.

$$P(x, t) = \mathbf{A}_{up} e^{i\left(\omega t + \frac{\omega(x-x_{out})}{|c-U|} + \Phi_{up}\right)} + \mathbf{A}_{dwn} e^{i\left(\omega t - \frac{\omega(x-x_{out})}{|c+U|} + \Phi_{dwn}\right)} \quad (1)$$

The amplitude and phase distributions of the respective travelling pressure waves are plotted in figure 7. According to the present decomposition, the amplitude \mathbf{A}_{up} and phase angle Φ_{up} of a single upstream travelling wave should be constant since time and spatial fluctuations are correlated in travelling waves. This is typically the case in the outflow region (from $x=230\text{mm}$ to 310mm) where the amplitude and phase angle were found fairly constant for both upstream and downstream propagating waves. At the outlet plane for instance, the acoustic field is mainly composed by upstream propagating wave since the amplitude of downstream propagating waves is nearly zero.

As suspected in the region downstream of the shock, the decomposition revealed the presence of both upstream and downstream propagating waves with respective amplitude 1.7 and 0.8. The relative phase angle distribution is more delicate to understand. For upstream propagating wave, the phase distribution tends to increase in the vicinity of the shock. This might be explained by the fact that the relative propagating velocity $|c-U|$ tends toward zero in the vicinity of the shock. The wave length thus also tends toward zero locally, which is interpreted as an increase of the phase in the decomposition algorithm. Concerning the downstream propagating waves, it is not yet clear why the phase distribution is decreasing between $x=80\text{mm}$ and $x=210\text{mm}$. It is assumed that the decomposition model is not fully accurate in the region and that other phenomena are not yet taken into account.

Unsteady pressure distribution at different channel heights. Considering the fairly good agreement between experiments and 2D RANS simulations, a complementary analysis of the unsteady pressure distribution was conducted within the numerical domain at different positions in the channel's height. In addition to the upper and lower walls, three other locations were selected as illustrated in figure 2(c): the SBLI region (probe C), the middle of the shock (probe B), and the region where the sonic line meets the shock (probe A).

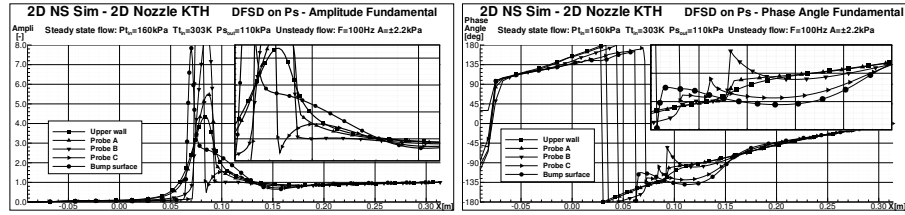


Figure 8. DFSD on unsteady pressure distribution over 2D bump for $F_p=100\text{Hz}$

At low perturbation frequency (100Hz), the highest pressure amplification occurs in the BL on the upper and lower walls. Although not located in the BL, a slight amplification occurs downstream of the shock at the location of probe A and C whereas the pressure amplification in the middle of the channel (probe B) is very similar to the one observed in Euler computation. Beside, the phase angle distribution exhibits the behaviour described previously concerning the increasing phase angle downstream of the shock exclusively for the location where a shock occurs. It is noteworthy that this phenomenon is most pronounced in the middle of the channel although no pressure amplification was noticed. It thus seems as the observed phenomenon on the phase angle is rather due to the presence of the shock wave than to viscous or turbulent effects.

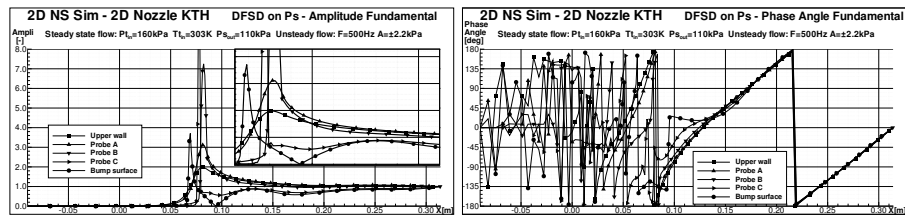


Figure 9. DFSD on unsteady pressure distribution over 2D bump for $F_p=500\text{Hz}$

At higher perturbation frequency (500Hz), a pressure attenuation can be observed close to the bump surface whereas a slight amplification still occurs at other location in the channel. Surprisingly, the increasing phase angle behaviour only occurs on the bump surface whereas the phase angle distribution reflects a single upstream propagating wave behaviour at all other locations.

The particular amplitude and phase angle distribution is not yet clearly understood and might be related to the lower amplitude of the motion of the

shock, its inertia to oscillate, or the smaller wave length of the perturbation at higher frequencies.

Shock motion. The amplitude and phase angle of the shock motion throughout the channel's height are presented in figure 10 and 11 respectively for the perturbation frequencies 100Hz and 500Hz. A fairly good agreement is achieved between experiments and numerics regarding both the amplitude and phase distribution of the unsteady shock motion. For both frequencies, the amplitude of shock motion increases with the height of the channel. It is noteworthy that the same trend is observed also in the Euler simulation. The amplitude of motion of the shock is thus related to the mean flow gradients rather than to the SBLI. Beside, the amplitude clearly decreases with the frequency. Assuming that the shock has a certain inertia to oscillate or to respond to a back pressure variation, the decreasing amplitude of motion of the shock at higher frequencies is then probably due to shorter perturbation wave length although the amplitude of perturbation remains the same.

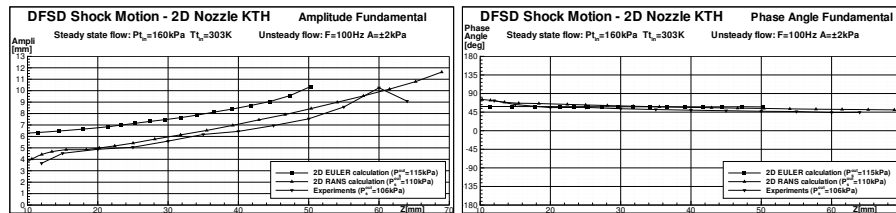


Figure 10. DFSD on shock motion over 2D bump for $F_p=100\text{Hz}$

On the other hand, the shock motion phase angle slightly differs both between the two frequencies and the two numerical calculations. At low frequency, the phase angle seems to be constant throughout the channel height, which corresponds to a "rigid" motion between the foot and the top of the shock. At higher frequency however, there is an important phase lag (up to 90° for experiments) between the foot and the top of the shock. The "head" of the shock seems to oscillate with a certain time lag (delay) compared to the foot. This tendency can be observed both on experimental visualization and 2D RANS simulation, but not on Euler calculation where the phase angle is still constant throughout the channel height. This effect might be related to the higher propagation speed within the BL than in the free stream. As a result, the pressure perturbations reach the foot of the shock slightly in advance in the SBLI region. The same behaviour should theoretically also be seen at lower frequencies, but since the wave propagation speed is the same, the perturbations wave length is longer and thus the phase lag between perturbations in the BL and in the free stream is lower.

Relation between unsteady pressure and shock motion. The phase lag between unsteady pressure distribution over the bump and the shock motion

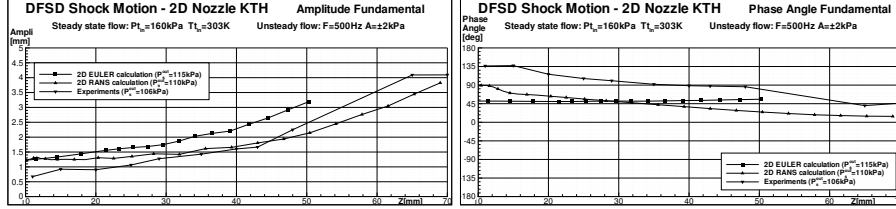


Figure 11. DFSD on shock motion over 2D bump for $F_p=500\text{Hz}$ (closest from the bump) has been calculated and plotted in figure 12 as a function of the perturbation frequency. Experimental results show an increasing phase lag with the perturbation frequency, meaning that the shock response with a certain increasing time delay with the perturbation frequency. For numerical simulation however, the trend is not as clear and further calculations should be performed in order to clearly define a tendency.

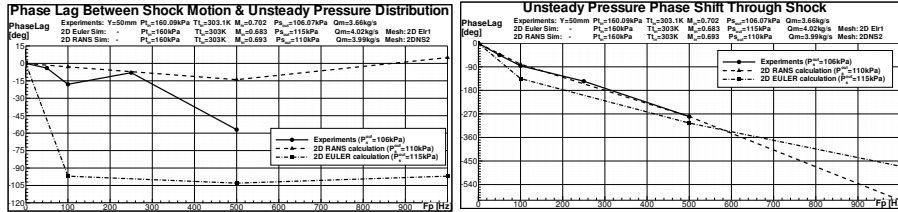


Figure 12. Phase Lag between P_s & Shock Figure 13. Phase shift through shock

Additionally, the unsteady pressure phase angle jump through underneath the shock location was plotted as a function of the perturbation frequency in figure 13. A fairly good agreement was found between experimental pressure measurements and 2D RANS numerical simulation. This unsteady pressure phase shift, which seems to increase linearly with the perturbation frequency, is extremely important considering aeroelastic stability prediction. Indeed, the unsteady aerodynamic load on an airfoil is directly influenced by the value of the phase shift and the overall stability of the airfoil might change from stable to unstable (and vice versa) for a certain value of this phase shift.

Unsteady separated region motion. The unsteady motion of the separated zone was evaluated as a function of the shock motion for the 2D RANS numerical simulation, and is presented in figure 14 for two perturbation frequencies (100Hz and 500Hz). The advantage to display the separation versus the shock motion is to be able to see both the amplitude of motion and the phase lag between the separation/reattachment and the shock oscillations. Clearly, the separation oscillates with the same amplitude and nearly in phase with the shock wave. This behaviour does not seem to change with the frequency and confirms the idea of a shock induced separation. On the other hand, the reattachment seems to oscillate with a much larger amplitude and a certain phase lag with the shock. Both the amplitude and phase lag seem to be related to the perturbation frequency. It is however not possible to state upon a clear ten-

dependency and further calculation as well as experimental measurement should be performed.

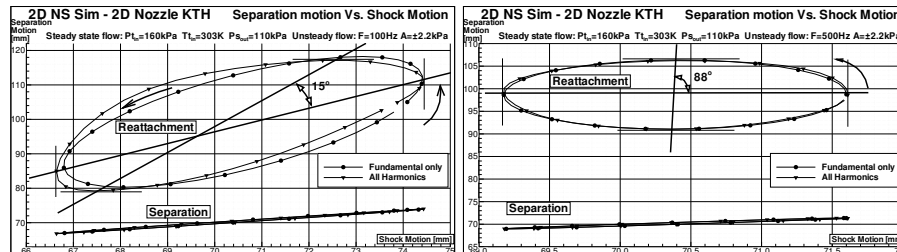


Figure 14. Separated region motion for 2D RANS calculations

4. Summary

Unsteady pressure measurements and high speed Schlieren visualizations were conducted together with 2D RANS and Euler numerical simulations over a convergent divergent nozzle geometry in order to investigate the Shock Boundary Layer interaction. A fairly good agreement between experiments and numerical simulations was obtained both regarding the unsteady pressure distribution and shock motion.

Results showed that the unsteady pressure distributions, both on the bump and within the channel, result from the superposition of upstream and downstream propagating waves. It is believed that outlet pressure perturbations propagate upstream within the the nozzle, interact in the high subsonic flow region according to the acoustic blockage theory, and are partly reflected or absorbed by the oscillating shock, depending on the frequency of the perturbations. The amplitude of motion of the shock was found to be related to the mean flow gradients and the local wave length of the perturbations rather than to the shock boundary layer interaction. The phase angle between unsteady pressure distribution on the bump and the shock motion for experimental results was found to increase with the perturbation frequency. However, no clear tendency could be defined for numerical results.

At last, but not least, the phase angle "jump" underneath the shock location was found to linearly increase with the perturbation frequency. The phase shift is critical regarding aeroelastic stability since it might have a significant impact on the phase angle of the overall aerodynamic force acting on the blade and shift the aerodynamic damping from stable to exciting.

Acknowledgments

The authors wish to thank the Swedish Energy Agency (STEM) for its financial support over the project, as well as the Center for Parallel Computers (PDC) and the National Informatic Center of Superior Education (CINES) for the CPU resources allowed.

Appendix: Two dimensional bump coordinates

Table A.1. Two-dimensional bump profile coordinates

x*	thickness*	x	thickness	x	thickness	x	thickness
-70.00	0.00	26.29	7.50	61.11	9.82	95.94	4.92
-56.51	0.00	29.19	8.39	64.01	9.56	98.84	4.47
-43.11	0.00	32.09	9.07	66.92	9.25	101.96	4.01
-29.72	0.00	34.99	9.59	69.82	8.91	107.25	3.29
-16.39	0.00	37.90	9.97	72.72	8.54	117.22	2.16
-5.13	0.00	40.80	10.24	75.62	8.13	131.71	1.02
3.45	0.06	43.70	10.40	78.52	7.70	146.34	0.37
9.78	1.01	47.60**	10.47	81.43	7.25	160.98	0.09
14.33	2.53	49.50	10.46	84.33	6.79	175.61	0.01
17.58	3.89	52.41	10.38	87.23	6.32	190.24	0.00
20.48	5.18	55.31	10.24	90.13	5.85	204.88	0.00
23.39	6.41	58.21	10.05	93.04	5.38	220.00	0.00

*Coordinates in mm. **Throat located at x=47.6mm.

References

- [1] DAVID S.S., MALCOM G.N. *Experiments in unsteady transonic flows* AIAA/ASME/ASCE/AHS 20th Structure, Structural Dynamics and Material Conference AIAA paper 79-769, pp. 417-433 St. Louis, M.O., 1979
- [2] ATASSI H.M., FANG J., FERRAND P. *A study of the unsteady pressure of a cascade near transonic flow condition* ASME paper 94-GT-476, June 1994
- [3] TIJDMAN H., SEEBASS R. *Transonic flow past oscillating airfoils* Annual Review of Fluid Mechanics, vol. 12, 1980, pp. 181-222
- [4] FERRAND P. *Etude theorique des ecoulements instationnaires en turbomachine axiale. Application au flottement de blocage* State thesis, Ecole Centrale de Lyon, 1986
- [5] EKATERINARIS J., PLATZER M. *Progress in the Analysis of Blade Stall Flutter* Symposium on Unsteady Aerodynamics and Aeroelasticity of Turbomachines, Tanida and Namba Editors, Elsevier, September 1994, pp. 287-302
- [6] ATASSI H.M., FANG J., FERRAND P. *Acoustic blockage effect in unsteady transonic nozzle and cascade flows* Symposium on Unsteady Aerodynamics and Aeroelasticity of Turbomachines, Tanida and Namba Editors, Elsevier, September 1994, pp. 777-794
- [7] OTT P. *Oszillierender Senkrechter Verdichtungsstoß in einer Ebenen Düse* Ph.D. Thesis at Ecole Polytechnique Federale de Lausanne; These No 985 (1991); 1992
- [8] FERRAND P., ATASSI H.M., AUBERT S. *Unsteady flow amplification produced by upstream or downstream disturbances* AGARD, CP 571, January 1996, pp. 331.1-31.10
- [9] FERRAND P., ATASSI H.M., SMATI L. *Analysis of the non-linear transonic blockage in unsteady transonic flows* AIAA paper 97-1803, Snowmass, Col. USA, 1997
- [10] FERRAND P., AUBERT S., ATASSI H.M. *Non-linear interaction of upstream propagating sound with transonic flows in a nozzle* AIAA paper 98-2213, Toulouse, France, 1998
- [11] GEROLYMOS G. A., BRUS J.P. *Computation of Unsteady Nozzle Flow due to Fluctuating Back-Pressure using Euler Equations* ASME Paper No. 94-GT-91
- [12] SMATI L. *Contribution au développement d'une méthode numérique d'analyse des écoulements instationnaires. Applications aux turbomachines* PhD Thesis, ECL, France, 1997